

Less is More: Decoder-Free Masked Modeling for Efficient Skeleton Representation Learning

Jeonghyeok Do[Ⓛ], Yun Chen[Ⓛ], Geunhyuk Youk[Ⓛ], and Munchurl Kim[Ⓛ]

Korea Advanced Institute of Science and Technology, South Korea
 {ehwjdgur0913, cyruby, rmsgurkjg, mkimee}@kaist.ac.kr
https://kaist-viclab.github.io/SLiM_site/

Abstract. The landscape of skeleton-based action representation learning has evolved from Contrastive Learning (CL) to Masked Auto-Encoder (MAE) architectures. However, each paradigm faces inherent limitations: CL often overlooks fine-grained local details, while MAE is burdened by computationally heavy decoders. Moreover, MAE suffers from severe computational asymmetry—benefiting from efficient masking during pre-training but requiring exhaustive full-sequence processing for downstream tasks. To resolve these bottlenecks, we propose **SLiM** (Skeleton Less is More), a novel unified framework that harmonizes masked modeling with contrastive learning via a shared encoder. By eschewing the reconstruction decoder, SLiM not only eliminates computational redundancy but also compels the encoder to capture discriminative features directly. **SLiM** is the *first* framework with *decoder-free masked modeling* of representative learning. Crucially, to prevent trivial reconstruction arising from high skeletal-temporal correlation, we introduce *semantic tube masking*, alongside *skeletal-aware augmentations* designed to ensure anatomical consistency across diverse temporal granularities. Extensive experiments demonstrate that SLiM consistently achieves state-of-the-art performance across all downstream protocols. Notably, our method delivers this superior accuracy with exceptional efficiency, reducing inference computational cost by $7.89\times$ compared to existing MAE methods.

Keywords: Skeleton-based self-supervised learning · Decoder-free unified framework · Semantic tube masking · Skeleton-aware augmentation

1 Introduction

Skeleton data serves as a compact yet informative modality for human action understanding, offering inherent robustness against dynamic backgrounds, lighting variations, and viewpoint shifts compared to RGB-based counterparts [15, 33, 40]. While supervised learning on skeleton data [4, 6, 9] has achieved remarkable success, it faces fundamental hurdles: beyond the prohibitive cost of large-scale annotation, supervised models often struggle with generalization, frequently overfitting to specific domain distributions and failing to adapt to unseen scenarios.

Consequently, Self-Supervised Learning (SSL) [2, 3, 12, 24, 42] has emerged as the dominant methodology to learn generalizable motion representations from

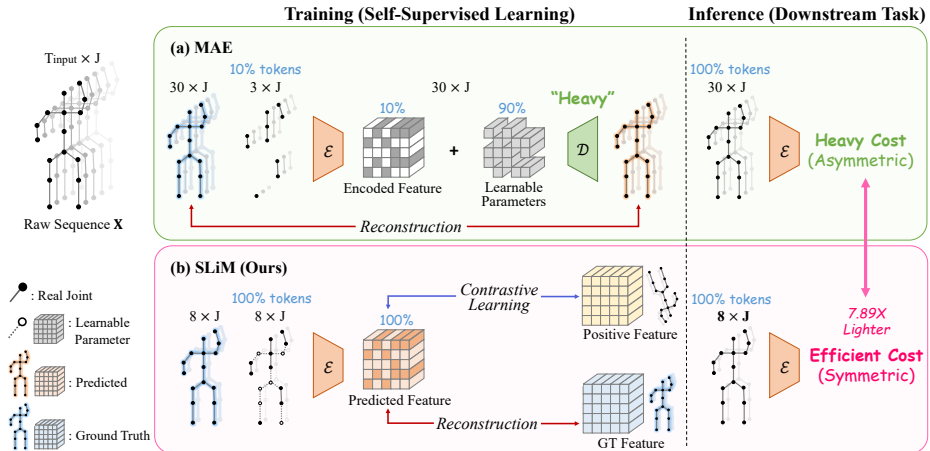


Fig. 1: Conceptual comparison of previous MAE methods and our SLiM. (a) Standard MAE methods suffer from a $14.38\times$ computational surge during inference relative to pre-training due to asymmetric full-sequence processing. (b) SLiM synergizes masked modeling with contrastive learning in a decoder-free framework. This symmetric design achieves a $7.89\times$ reduction in inference cost compared to MAE baselines.

abundant unlabeled data. The evolution of SSL in skeleton analysis has primarily shifted from Contrastive Learning (CL) [3] to Masked Auto-Encoder (MAE) [12] architectures. Early CL approaches [11, 17, 23, 39] focused on instance discrimination, pulling augmented views of the same sequence together. However, CL relies heavily on global pooling, which often leads to the *vanishing local details* problem—overlooking fine-grained motion patterns crucial for complex actions—and suffers from the difficulty of constructing semantically consistent pairs.

To mitigate this, recent trends have pivoted towards MAE frameworks [1, 22, 32, 38] that learn by reconstructing masked input patches. Although MAE excels at capturing local dependencies, it introduces severe computational inefficiencies rooted in its architectural design. Fig. 1 shows a conceptual comparison of previous MAE methods and ours. In Fig. 1-(a), standard MAE frameworks adopt an asymmetric encoder-decoder structure. During pre-training, they mask a massive ratio (e.g., 90%) of input tokens and feed only a small subset of visible tokens into the encoder. Before passing these features to the decoder, the missing positions are filled with learnable mask tokens to restore the full sequence length. This design leads to two distinct computational hurdles: (i) the *heavy decoder problem* — unlike the lightweight encoder, the decoder must process the full sequence (100%) to reconstruct the original input, consuming significant resources; (ii) more critically, this entails a drastic *computational asymmetry* between pre-training and downstream application. While the pre-training encoder load is kept artificially light, downstream tasks require processing the full, unmasked sequence. Consequently, the computational cost surges disproportionately during inference—inflating the encoder’s burden by over $14.38\times$ compared

Table 1: Efficiency and performance comparison on NTU-60. SLiM achieves state-of-the-art accuracy while reducing inference computational cost by 7.89× compared to MAE methods. TGN: Target Generation Network. **Bold** indicates the best result.

Methods	Venue	Loss	Tokens	Inference (GFLOPs)	Training (GFLOPs)			NTU-60 (Acc, %)	
			$T \times J$	Encoder	Encoder	Decoder	TGN	X-Sub	X-View
SkeletonMAE [38]	ICCV'23	MAE	30×25	28.32	1.97	17.70	–	74.8	77.7
MAMP [22]	ICCV'23	MAE	30×25	28.32	1.97	17.70	–	84.9	89.1
S-JEPA [1]	ECCV'24	MAE	30×25	28.32	1.97	17.70	28.32	85.3	89.8
GFP [32]	ICCV'25	MAE	30×25	28.32	1.97	1.57	0.64	85.9	92.0
SLiM (Ours)		MAE + CL	8×25	3.59	3.59	–	3.59	87.9	93.2

to the pre-training phase. This renders standard MAE encoders prohibitively expensive for real-world deployment.

To bridge the gap between efficiency and representation quality, we propose **SLiM** (**S**keleton **L**ess is **M**ore), a novel unified *decoder-free* framework that synergizes the strengths of masked modeling (MAE) and contrastive learning (CL). Unlike previous approaches that treat them separately, SLiM integrates them into a single, shared encoder architecture (Fig. 1-(b)). Our key insight is to replace the computationally heavy reconstruction decoder with a lightweight, feature-level masking objective. Specifically, SLiM employs a teacher–student distillation setup where the student encoder sees masked views and predicts the teacher’s features of the full view. This design not only resolves the computational bottleneck by removing the decoder but also enables the shared encoder to simultaneously optimize for two complementary objectives: instance discrimination (CL) for global semantic invariance and feature reconstruction (MAE) for fine-grained local context understanding. Table 1 shows that SLiM achieves superior performance and efficiency, surpassing the latest MAE methods in accuracy with a 7.89× reduction in inference cost.

However, blindly applying masked modeling to skeleton data is suboptimal due to the high skeletal-temporal correlation of human joints. Independent joint masking often allows the model to cheat by simply interpolating missing joints from neighbors without understanding the underlying action semantics. To prevent this, we adopt a *Semantic Tube Masking* strategy that masks integral body parts across temporal segments, forcing the encoder to infer motion dynamics from global context rather than local coordinates. Furthermore, to maximize the efficacy of the contrastive branch, we propose a suite of improved *Skeletal-Aware Augmentations*. By generating diverse yet anatomically consistent views—ranging from skeleton-aware rotation and mirroring to bone-aware scaling and variable temporal sampling—we facilitate the construction of real-world plausible pairs. This enables the model to capture invariant representations that are inherently robust to significant viewpoint shifts, scale variations, and speed changes. Our main contributions are summarized as follows:

- We introduce **SLiM**, a novel *decoder-free* framework by eliminating the heavy reconstruction decoder and adopting a symmetric token processing

design, SLiM fundamentally resolves the *computational asymmetry* and inference overhead inherent in standard MAE architectures.

- We propose a *unified representation learning architecture* that synergizes the global discriminative power of contrastive learning with the local context sensitivity of masked modeling through a single, shared encoder.
- To mitigate shortcut reconstruction caused by the high correlation among skeletal joints, we adopt **Semantic Tube Masking** alongside refined **Skeleton-Aware Augmentations** which force the encoder to capture deeper action semantics.
- Extensive experiments demonstrate that our SLiM consistently achieves state-of-the-art performance *across all downstream protocols*, while simultaneously providing a *7.89× reduction* in inference computational cost compared to existing MAE methods.

2 Related Works

2.1 Contrastive learning (CL)-based Approaches

Early self-supervised approaches primarily utilized CL [3] to capture discriminative global features via instance discrimination. CrosSCLR [45] introduced a cross-view consistency constraint to learn view-invariant representations, while AimCLR [11] enhanced robustness through extreme augmentations. To incorporate richer semantics, HaLP [25] proposed latent positive mining, and ActCLR [17] decomposed actions into static and dynamic components. However, these frameworks often rely on generic spatial transformations that overlook anatomical constraints.

2.2 Masked auto-encoder (MAE)-based Approaches

MAE [12] approaches have recently shifted the focus toward reconstructing masked inputs to learn detailed skeletal-temporal dependencies. SkeletonMAE [38] established the first skeleton-based MAE framework by reconstructing masked joint coordinates to capture spatial topology. MAMP [22] advanced this by targeting motion-aware trajectories, encouraging the model to learn complex temporal dynamics. S-JEPA [1] moved beyond low-level reconstruction by employing a joint embedding predictive architecture that operates in the latent feature space. GFP [32] introduced a generative feature prediction task to bridge the gap between local reconstruction and high-level semantic understanding. While these methods have evolved from random masking [38] to motion-aware masking [1, 22, 32] strategies, they fundamentally rely on independent joint masking. Due to strong dependencies between skeletal joints, such an approach often allows models to simply interpolate missing joints from their immediate neighbors.

2.3 Other Pretext Tasks

Beyond CL and MAE, other emerging paradigms have explored generative and fusion-based strategies. MacDiff [37] and IGM [16] leverage diffusion-based generative processes to learn robust action representations by denoising skeletal sequences through iterative refinement. In terms of multi-modal integration, HSP [35] proposes a hierarchical semantic preservation framework that fuses 2D and 3D skeleton data to exploit complementary geometric and appearance cues. While these methods offer unique perspectives, they often require complex sampling or multi-stream inputs (e.g., bone or motion modalities). In contrast, SLiM achieves both superior performance and higher efficiency using a minimalist single-stream architecture focused solely on 3D joint-modality inputs.

3 Method

3.1 Overview of SLiM

Fig. 2 illustrates our **SLiM** (Skeleton Less is More), a unified framework that seamlessly integrates masked modeling with contrastive learning without relying on a computationally heavy reconstruction decoder. The SLiM architecture adopts a teacher–student distillation scheme [34]. Specifically, the student network f_{θ} , parameterized by θ , is trained via back-propagation. The teacher network f_{ϕ} , parameterized by ϕ , is not updated by gradients but evolves via an Exponential Moving Average (EMA) [34] of the student weights: $\phi \leftarrow \tau\phi + (1-\tau)\theta$, where τ is a momentum coefficient. Both networks share the identical architecture, consisting of an encoder g and lightweight (3-layer MLP) prediction heads h_{CL} and h_{MAE} .

Architecture of encoder. We employ a Vision Transformer (ViT) [8] as the backbone encoder g . Let the input skeleton sequence be denoted as $\mathbf{X} \in \mathbb{R}^{T \times J \times C_{\text{in}}}$, where T is the sequence length, J is the number of joints, and $C_{\text{in}} (= 3)$ is the joint dimension. We reshape it into a sequence of flattened 2D patches $\mathbf{X}_p \in \mathbb{R}^{N \times D_p}$, where $N = (T/P_T) \times (J/P_J)$ is the number of patches and $D_p = P_T \cdot P_J \cdot C_{\text{in}}$ is the raw patch dimension. Here, (P_T, P_J) denotes the resolution of each skeletal-temporal patch. To effectively capture the skeletal-temporal dynamics, we utilize a composite embedding strategy. First, we apply a linear projection $\mathbf{E} \in \mathbb{R}^{D_p \times D}$ to \mathbf{X}_p and add absolute joint positional embeddings $\mathbf{E}_{\text{skel}} \in \mathbb{R}^{(J/P_J) \times D}$ to encode the identity of each joint:

$$\mathbf{Z}_p = [\mathbf{x}_p^1 \mathbf{E} \mid \mathbf{x}_p^2 \mathbf{E} \mid \dots \mid \mathbf{x}_p^N \mathbf{E}] + \mathbf{E}_{\text{skel}}^b, \quad (1)$$

where $\mathbf{Z}_p \in \mathbb{R}^{N \times D}$ represents the sequence of patch tokens and D is the embedding dimension. $\mathbf{E}_{\text{skel}}^b \in \mathbb{R}^{N \times D}$ is a broadcast version of \mathbf{E}_{skel} along the temporal dimension to match the sequence length N . We append a learnable class token $\mathbf{z}_{\text{cls}} \in \mathbb{R}^{1 \times D}$ to the patch tokens \mathbf{Z}_p , initializing the input sequence $\mathbf{Z}_0 = [\mathbf{z}_{\text{cls}} \mid \mathbf{Z}_p]$. Second, to explicitly model temporal dependencies, we adopt 1D

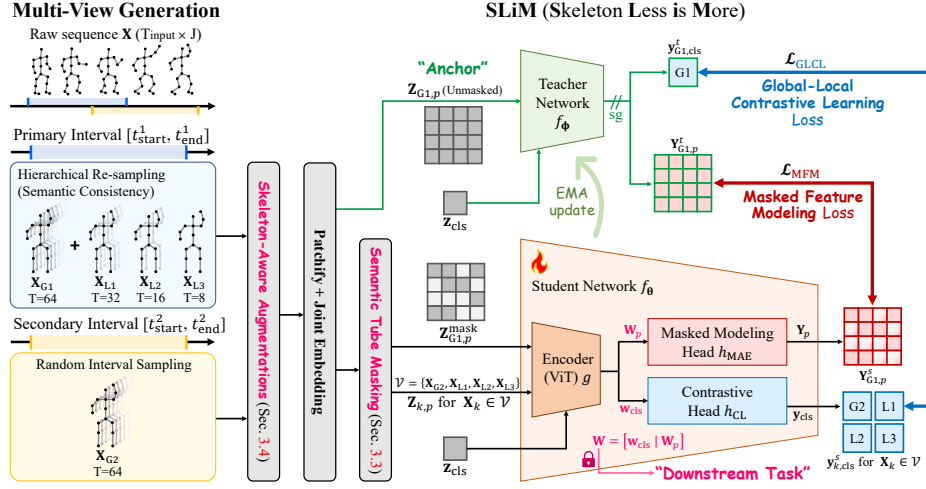


Fig. 2: Overview of SLiM. Our framework unifies Masked Feature Modeling and Global-Local Contrastive Learning within a decoder-free teacher–student architecture. The student encoder simultaneously minimizes the feature reconstruction error (\mathcal{L}_{MFM}) on masked patches and the contrastive loss ($\mathcal{L}_{\text{GLCL}}$) across diverse local views, effectively capturing both fine-grained patterns and global semantics.

temporal rotary positional embeddings (RoPE) [27]. RoPE is injected directly into the attention mechanism at each layer:

$$\begin{aligned}
 \mathbf{Z}_0 &= [\mathbf{z}_{\text{cls}} \mid \mathbf{Z}_p], & \text{Input initialization} \\
 \mathbf{Z}'_l &= \text{MSA}(\text{LN}(\mathbf{Z}_{l-1})) + \mathbf{Z}_{l-1}, & \text{Attention w/ temporal RoPE} \\
 \mathbf{Z}_l &= \text{MLP}(\text{LN}(\mathbf{Z}'_l)) + \mathbf{Z}'_l, & l = 1, 2, \dots, L \\
 \mathbf{W} &= [\mathbf{w}_{\text{cls}} \mid \mathbf{W}_p] = \text{LN}(\mathbf{Z}_L), & \text{Final skeleton representation}
 \end{aligned} \tag{2}$$

where MSA denotes Multi-Head Self-Attention, LN is Layer Normalization, MLP is a feed-forward network, L is the number of layers, and \mathbf{W} denotes the final skeleton representation leveraged for downstream evaluation. Unlike absolute learnable embeddings that require interpolation for varying sequence lengths, RoPE naturally generalizes to diverse temporal views (e.g., spanning 8 to 64 frames) generated by our multi-view generation strategy (Sec. 3.4), thereby preserving relative temporal dependencies robustly.

Prediction heads. They are depicted in the light red and blue boxes of student network f_θ in Fig. 2. The encoder output \mathbf{W} is split into the global representation \mathbf{w}_{cls} and patch-wise local representations \mathbf{W}_p . These are fed into two separate lightweight heads (3-layer MLPs): h_{CL} and h_{MAE} . The Contrastive Head h_{CL} projects \mathbf{w}_{cls} for the instance discrimination objective, producing $\mathbf{y}_{\text{cls}} = h_{\text{CL}}(\mathbf{w}_{\text{cls}})$. Simultaneously, the Masked Modeling Head h_{MAE} projects the patch features \mathbf{W}_p to the target latent space as $\mathbf{Y}_p = h_{\text{MAE}}(\mathbf{W}_p)$.

3.2 Decoder-Free Masked Modeling with Contrastive Learning

Multi-view generation strategy. To learn robust representations across varying temporal granularities, we employ a hierarchical temporal sampling strategy. We first generate two global views ($\mathbf{X}_{G1}, \mathbf{X}_{G2}$) by randomly selecting temporal intervals $[t_{\text{start}}^1, t_{\text{end}}^1]$ for \mathbf{X}_{G1} and $[t_{\text{start}}^2, t_{\text{end}}^2]$ for \mathbf{X}_{G2} . Contrasting these randomized global views encourages the model to learn instance-level invariance, ensuring robust recognition of the action identity even across temporally distant segments. For hierarchical temporal sampling, we generate local views ($\mathbf{X}_{L1}, \mathbf{X}_{L2}, \mathbf{X}_{L3}$) by strictly re-sampling from the *same* temporal interval $[t_{\text{start}}^1, t_{\text{end}}^1]$ assigned to the primary global view \mathbf{X}_{G1} , with reduced resolutions of 32, 16, and 8 frames. This constraint is vital because random sampling across the entire skeleton sequence can lead to *semantic misalignment*—where two views from the same sequence (e.g., the beginning vs. the end) share no temporal overlap and depict completely different motion states. By anchoring local views to the global interval, we guarantee semantic consistency, driving the model to learn *temporal scale invariance* rather than matching unrelated motion segments. All views are subsequently processed by the skeleton-aware augmentations (Sec. 3.4). We symmetrize the training objective by repeating this multi-view generation process with \mathbf{X}_{G2} as the anchor and aggregating the bidirectional losses.

Decoder-free masked feature modeling (MFM). We formulate the masked modeling objective as a feature prediction task within the distillation process. The primary global view \mathbf{X}_{G1} serves as the anchor. The teacher network f_ϕ receives the unmasked input \mathbf{X}_{G1} to generate the target latent representations: $[\mathbf{y}_{G1, \text{cls}}^t \mid \mathbf{Y}_{G1, p}^t] = f_\phi([\mathbf{z}_{\text{cls}} \mid \mathbf{Z}_{G1, p}])$. For the student network f_θ , we apply a binary mask $\mathcal{M} \in \{0, 1\}^N$ (generated via Semantic Tube Masking in Sec. 3.3) to the patch tokens of the same view. The masked input $\mathbf{Z}_{G1, p}^{\text{mask}}$ is defined as:

$$\mathbf{Z}_{G1, p}^{\text{mask}} = \mathcal{M} \odot \mathbf{Z}_{G1, p} + (1 - \mathcal{M}) \odot \mathbf{e}_{[\text{mask}]}, \quad (3)$$

where $\mathbf{e}_{[\text{mask}]} \in \mathbb{R}^D$ is a learnable mask token vector, and $\mathbf{e}_{[\text{mask}]}^b \in \mathbb{R}^{N \times D}$ is broadcast version. The student then predicts the features of the masked patches: $[\mathbf{y}_{G1, \text{cls}}^s \mid \mathbf{Y}_{G1, p}^s] = f_\theta([\mathbf{z}_{\text{cls}} \mid \mathbf{Z}_{G1, p}^{\text{mask}}])$. Following the iBOT framework [42], we employ the cross-entropy loss between f_θ 's prediction and f_ϕ 's target distribution on the masked patches. The masked feature modeling loss is defined as:

$$\mathcal{L}_{\text{MFM}} = - \sum_{i \in \text{masked}} \mathbf{p}_{G1, p}^t(i) \log \mathbf{p}_{G1, p}^s(i), \quad (4)$$

where $\mathbf{p}_{G1, p}^t$ and $\mathbf{p}_{G1, p}^s$ are the probability distributions obtained by applying softmax to the teacher and student patch token outputs $\mathbf{Y}_{G1, p}^t$ and $\mathbf{Y}_{G1, p}^s$, respectively. This fully *decoder-free* design eliminates the heavy reconstruction bottleneck, while the use of mask tokens ensures a symmetric computational flow that prevents inference-time complexity surges inherent in previous MAEs.

Global-local contrastive learning (GLCL). Similar to masked modeling, we utilize the global view \mathbf{X}_{G1} as the primary anchor to guide the representation learning of other views. Let $\mathbf{y}_{G1, \text{cls}}^t$ denote the teacher's global class token output.

We generate the student’s features for a set of the corresponding local and global views $\mathcal{V} = \{\mathbf{X}_{G2}, \mathbf{X}_{L1}, \mathbf{X}_{L2}, \mathbf{X}_{L3}\}$ as:

$$[\mathbf{y}_{k,\text{cls}}^s \mid \mathbf{Y}_{k,p}^s] = f_{\theta}([\mathbf{z}_{\text{cls}} \mid \mathbf{Z}_{k,p}]), \quad \mathbf{X}_k \in \mathcal{V}. \quad (5)$$

It is reminded that local views ($\mathbf{X}_{L1}, \mathbf{X}_{L2}, \mathbf{X}_{L3}$) are sampled from the same interval of \mathbf{X}_{G1} . The contrastive loss [2, 5, 24] is minimized by matching the student’s predictions for all views $\mathbf{X}_k \in \mathcal{V}$ to the teacher’s anchor distribution:

$$\mathcal{L}_{\text{GLCL}} = - \sum_{\mathbf{X}_k \in \mathcal{V}} \mathbf{p}_{G1,\text{cls}}^t \log \mathbf{p}_{k,\text{cls}}^s, \quad (6)$$

where $\mathbf{p}_{G1,\text{cls}}^t$ and $\mathbf{p}_{k,\text{cls}}^s$ denote the probability distributions obtained by applying softmax to the teacher and student class token outputs, $\mathbf{y}_{G1,\text{cls}}^t$ and $\mathbf{y}_{k,\text{cls}}^s$ respectively. This objective forces the student network f_{θ} to learn *temporal scale invariance* by aligning the representations of local fine-grained clips with the global semantic context provided by the teacher network f_{ϕ} .

Total objective. We train SLiM in an end-to-end manner by minimizing a unified objective function. The total loss $\mathcal{L}_{\text{total}}$ integrates the masked feature modeling loss \mathcal{L}_{MFM} with the global-local contrastive loss $\mathcal{L}_{\text{GLCL}}$:

$$\mathcal{L}_{\text{total}} = \mathcal{L}_{\text{MFM}} + \lambda \mathcal{L}_{\text{GLCL}}, \quad (7)$$

where λ is a hyperparameter balancing the two objectives, which is empirically set to 1.0. This joint optimization guides the student network f_{θ} to simultaneously capture fine-grained motion patterns through masked modeling and high-level semantic contexts through contrastive learning, resulting in robust and discriminative representations.

3.3 Semantic Tube Masking (STM)

Fig. 3-(a) and -(e) show an independent joint masking of previous methods [1, 22, 32, 38] and our masking strategy, respectively. Independent joint masking is often susceptible to trivial solutions due to the high correlation in skeleton sequences. To resolve this, we propose *Semantic Tube Masking (STM)*, a strategy that masks anatomical joint groups (e.g., left arm, right leg, or torso) continuously along the temporal axis, thereby forming a skeletal-temporal *tube*. Unlike prior masking schemes that treat joints as isolated tokens, STM imposes a more challenging pretext task by occluding entire functional units of the body over time. To our knowledge, SLiM is the first to adopt tube masking for skeleton data, providing a simple yet highly effective strategy for robust representation learning.

Skeletal-temporal tube design. STM ensures skeletal-temporal consistency by occluding a specific joint group across consecutive frames. We adopt a constant tube volume strategy: the temporal duration is adjusted inversely to the spatial size of the anatomical group. For instance, smaller groups (e.g., hands) are masked over longer temporal spans, while larger groups (e.g., entire limbs) are masked for shorter intervals. This constant-volume design effectively prevents

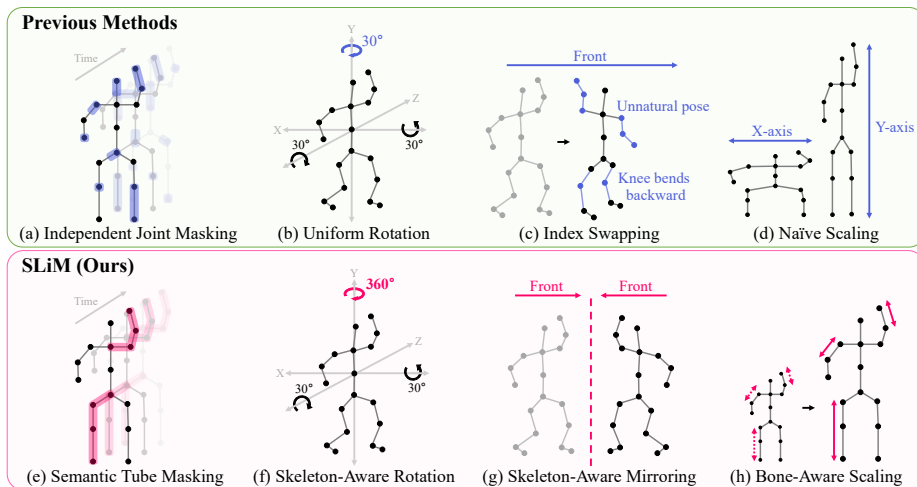


Fig. 3: Comparison of masking and augmentation strategies. *Top:* previous masking (a) and augmentations (b-d) resulting in trivial solutions or physically implausible poses. *Bottom:* our Semantic Tube Masking (e) and Skeletal-Aware Augmentations (f-h) ensuring anatomical and physical consistency through skeleton-aware designs.

naive coordinate interpolation, prompting the encoder to infer missing motion dynamics through global context and inter-part dependencies.

STM’s dual-role in training. Crucially, STM serves a dual-purpose masking in our framework: firstly, it generates the masked views for the masked feature modeling (MFM) objective; secondly, it functions as a hard structural augmentation for global-local contrastive learning (GLCL). For both purposes, the masking operation follows the formulation in Eq. 3, where the selected skeletal-temporal patch tokens are replaced by the shared learnable mask token $e_{[\text{mask}]}$.

3.4 Skeleton-Aware Augmentations (SAA)

Standard geometric augmentations [11, 17, 45] often disregard the articulated nature of the human body, leading to implausible poses or distorted limb proportions. We introduce *Skeletal-Aware Augmentations (SAA)*, a set of improved transformations designed to construct diverse yet structurally valid pairs.

Skeleton-aware rotation. This is illustrated in Fig. 3-(f) and compared with the uniform rotation in Fig. 3-(b). Standard rotation [4, 11, 17] is typically confined to a limited range of angles. To maintain a realistic upright posture, we apply a full 360° random rotation exclusively around the vertical Y -axis. For the remaining non-gravity axes (X, Z), we constrain perturbations to small angles (e.g., 30°) to avoid physically implausible tilting. Unlike previous works that restrict all axes to maintain stability, our approach decouples the rotation logic to maximize view diversity while preserving physical validity.

Skeleton-aware mirroring. As shown in Fig. 3-(g), and compared with the index swapping in Fig. 3-(c), heuristic index swapping [6, 11, 17] is a common ap-

proach but fails to achieve a mathematically rigorous reflection, thereby resulting in unnatural poses. Our strategy performs a geometric mirroring that simultaneously negates coordinate values along the lateral axis (X -axis) and reassigns joint indices according to bilateral symmetry. This dual-operation ensures that the resulting motion is anatomically consistent—preserving the correct “Front” orientation and left-right semantics—rather than producing a distorted artifact.

Bone-aware scaling. This is depicted in Fig. 3-(h) and compared with the naive scaling in Fig. 3-(d). The naive scaling of joint coordinates [4, 11] can disrupt the structure of the skeleton. To preserve the essence of the action, we decompose each bone into a directional unit vector $\hat{\mathbf{v}}$ and a scalar length l . We apply random scaling factors only to l while strictly maintaining $\hat{\mathbf{v}}$. This effectively simulates the same action performed by subjects of varying body sizes and proportions, thereby enriching the intra-class variance without semantic distortion.

4 Experimental Results

4.1 Datasets

We evaluate our SLiM on three large-scale benchmark datasets: NTU RGB+D 60 (NTU-60) [26], NTU RGB+D 120 (NTU-120) [19], and PKU-MMD II [18]. NTU-60 contains 56,880 skeleton sequences across 60 action classes, captured from three distinct camera views. It offers two evaluation protocols: Cross-Subject (X-Sub) and Cross-View (X-View). NTU-120 extends this to 120 classes and 114,480 samples, featuring Cross-Subject (X-Sub) and Cross-Setup (X-Set) protocols. PKU-MMD II encompasses 51 action classes; following standard practice, we utilize the skeleton modality under the Cross-Subject (X-Sub) protocol.

Focus on 3D skeleton. 2D skeleton sequences are typically extracted from images via pre-trained pose estimation networks [30] and inherently represent coordinates on the image plane. Consequently, they can easily achieve high performance by being back-projected onto the image space to leverage existing image-domain representations [9]. In contrast, 3D skeleton data encapsulates the pure geometric structure of human motion. Therefore, we focus our evaluation on 3D sequences to rigorously validate the model’s intrinsic geometric representation capability without any reliance on such image-domain priors.

4.2 Experiment Details

Architecture. To ensure a fair comparison with previous MAE-based methods [1, 22, 32, 38], we employ a standard ViT [8] as our backbone encoder g . The encoder g consists of 8 layers with a hidden dimension of $D = 256$ and 8 attention heads, maintaining an identical architectural complexity to existing baselines. Input skeleton sequences are fixed to a temporal length of $T = 64$ frames with $J = 25$ joints. For patch embedding, we adopt a skeletal-temporal patch size of $P_J = 1$ and $P_T = 8$.

Pre-training setup. Our SLiM is pre-trained for 150 epochs within a teacher–student distillation framework [34]. The teacher’s momentum τ is updated from

Table 2: Comparison with state-of-the-art methods under the *linear evaluation* on NTU-60, NTU-120, and PKU-MMD II datasets. Performance is reported as Top-1 accuracy (%). **Bold** indicates the best result, and underline indicates the second best.

Method	Venue	NTU-60		NTU-120		PKU-MMD II
		X-Sub	X-View	X-Sub	X-Set	X-Sub
<i>Other pretext task:</i>						
GL-Transformer [14]	ECCV'22	76.3	83.8	66.0	68.7	–
MacDiff [37]	ECCV'24	<u>86.4</u>	91.0	79.4	80.2	–
IGM [16]	ECCV'24	86.2	91.2	<u>80.0</u>	<u>81.4</u>	–
USDRL [36]	AAAI'25	85.2	91.7	76.6	78.1	54.4
HSP [35]	CVPR'25	80.7	88.0	71.0	73.2	48.9
<i>Contrastive learning (CL):</i>						
CPM [39]	ECCV'22	78.7	84.9	68.7	69.6	48.3
CMD [23]	ECCV'22	79.8	86.9	70.3	71.5	43.0
AimCLR [11]	AAAI'22	74.3	79.7	63.4	63.4	–
RVTCLR [44]	ICCV'23	74.7	79.1	–	–	–
PTSL [43]	AAAI'23	77.3	81.8	66.2	67.7	49.3
HYSP [10]	ICLR'23	78.2	82.6	61.8	64.6	–
HaLP [25]	CVPR'23	79.7	86.8	71.1	72.2	43.5
ActCLR [17]	CVPR'23	80.9	86.7	69.0	70.5	–
<i>Masked auto-encoder (MAE):</i>						
SkeletonMAE [38]	ICCV'23	74.8	77.7	72.5	73.5	36.1
MAMP [22]	ICCV'23	84.9	89.1	78.6	79.1	53.8
S-JEPA [1]	ECCV'24	85.3	89.8	79.6	79.9	53.5
GFP [32]	ICCV'25	85.9	<u>92.0</u>	79.1	80.3	<u>56.2</u>
<i>Unified framework (MAE + CL):</i>						
SLiM (Ours)		87.9	93.2	81.2	83.6	59.7

0.994 to 1. Optimization is performed using AdamW [21] with a base learning rate of 2.0×10^{-4} , incorporating a 20-epoch linear warmup followed by a cosine decay [20] down to 1.0×10^{-6} . We train the model with a total batch size of 768 across 4 NVIDIA RTX A6000 GPUs.

Masking and augmentations. During pre-training, the masking ratio for STM is randomly sampled between $p \in [0.5, 0.9]$ and applied identically across both of its dual roles. For our SAA, each transformation is applied with a probability of $p = 0.5$. Skeleton-aware rotation applies a full 360° rotation around the vertical Y -axis, with perturbations on non-gravity axes limited to 30° . Bone-aware scaling samples factors from $[0.85, 1.15]$, which are applied to bone lengths l while preserving the directional unit vectors \hat{v} .

4.3 Performance Comparison

We evaluate our SLiM against state-of-the-art self-supervised approaches, including CL, MAE, and other pretext tasks [14, 16, 35–37]. To ensure a fair comparison and isolate the efficacy of the learned representations, we report results based on the single joint modality across all baselines, excluding gains from multi-stream fusion (e.g., bone or motion modalities).

Table 3: Performance comparison under the *semi-supervised* setting on NTU-60. Results are reported using 1% and 10% labeled data for both X-Sub and X-View protocols.

Method	X-Sub		X-View	
	1%	10%	1%	10%
GL-Transformer [14]	–	68.6	–	74.9
CPM [39]	56.7	73.0	57.5	77.1
CMD [23]	50.6	75.4	53.0	80.2
HYSP [10]	–	76.2	–	80.4
HaLP [25]	46.6	72.6	48.7	77.1
HiCo [7]	54.4	73.0	54.8	78.3
UmURL [31]	58.1	–	58.3	–
USDRL [36]	57.3	80.2	60.7	84.0
SkeletonMAE [38]	54.4	80.6	54.6	83.5
MAMP [22]	66.0	88.0	68.7	91.5
S-JEPA [1]	67.5	88.4	69.1	91.4
GFP [32]	<u>71.8</u>	<u>88.7</u>	<u>72.9</u>	<u>92.1</u>
SLiM (Ours)	72.1	88.8	75.8	91.9

Table 4: Performance comparison for skeleton-based *action retrieval* on NTU-60. The evaluation is conducted for X-Sub and X-View protocols.

Methods	NTU-60	
	X-Sub	X-View
LongT-GAN [41]	39.1	48.1
P&C [28]	50.7	76.3
ISC [29]	62.5	82.6
HaLP [25]	65.8	83.6
HiCo [7]	68.3	84.8
SkeAttnCLR [13]	69.4	76.8
UmURL [31]	<u>71.3</u>	<u>88.3</u>
MAMP [22]	62.0	70.0
GFP [32]	70.9	87.1
SLiM (Ours)	72.5	89.9

Action recognition (linear evaluation). Table 2 reports the Top-1 accuracy under the standard linear evaluation [1, 22, 32]. In this setting, we freeze the parameters of the pre-trained encoder and train only a single-layer linear classifier for evaluation. While previous methods often showed inconsistent performance across different benchmarks, SLiM establishes a new state-of-the-art across multiple evaluated datasets: NTU-60, NTU-120, and PKU-MMD II. As shown in Table 2, our framework consistently outperforms *all* existing representation learning paradigms. Remarkably, as highlighted in Table 1, our performance gains are achieved with significantly reduced computational overhead, requiring only 3.59 GFLOPs for inference—a $7.89\times$ reduction in computational cost compared to traditional MAE methods. Specifically, on the large-scale NTU-120 benchmark, SLiM achieves 81.2% on X-Sub and 83.6% on X-Set, surpassing the previous best method by 1.2%-point and 2.2%-point, respectively. On NTU-60, our method demonstrates superior robustness with 87.9% on X-Sub and 93.2% on X-View, representing a significant lead over existing frameworks. Furthermore, SLiM sets a new record on the PKU-MMD II dataset with 59.7% on X-Sub. Across the five primary evaluation protocols, SLiM provides an average accuracy improvement of approximately 1.9%-point over the closest competitors.

Action recognition (semi-supervised learning). To evaluate the data efficiency and label robustness of the pre-trained representations, we conduct semi-supervised learning experiments on the NTU-60 dataset. Table 3 shows the performance comparison for action recognition under 1% and 10% label settings. For the experimental setup, we follow the standard evaluation protocol [1, 22, 32] by fine-tuning the pre-trained encoder using only these limited labeled subsets and measure the performance according to NTU-60. SLiM significantly outperforms MAE methods under the extremely label-sparse 1% setting, while the

Table 5: Ablation studies for the objective functions on NTU-60. \mathcal{L}_{MFM} denotes the MFM loss. \mathcal{L}_{CL} represents a standard CL loss *without temporal diversity*, while $\mathcal{L}_{\text{GLCL}}$ is GLCL loss incorporating diverse temporal sampling.

Objective			NTU-60	
\mathcal{L}_{MFM}	\mathcal{L}_{CL}	$\mathcal{L}_{\text{GLCL}}$	X-Sub	X-View
✗	✓	✗	73.6	78.9
✗	✗	✓	75.3	80.1
✓	✗	✗	85.3	90.6
✓	✓	✗	86.2	91.3
✓	✗	✓	87.7	92.7

Table 6: Ablation studies for the dual-role masking strategies within STM. We evaluate the synergy between applying masked modeling to the *Global View* and utilizing augmented *Local Views* for contrastive learning. Limited: previous motion-aware masking.

Masking (dual-role)		NTU-60	
Global View	Local View	X-Sub	X-View
✗	✓	75.3	80.1
✓ (Limited)	✓	84.2	90.4
✓	✗	83.3	89.4
✓	✓ (Limited)	85.7	89.9
✓	✓	87.7	92.7

performance gap narrows at 10%. This phenomenon stems from differences in sequence length, token density, and network capacity. Previous MAE models process $T = 120$ frames with a fine-grained temporal patch size of $P_T = 4$, resulting in extended token sequences that require extensive data to properly optimize. In contrast, SLiM utilizes $T = 64$ frames with a coarser patch size of $P_T = 8$, operating on merely $\sim 25\%$ of the tokens. Under extreme label sparsity (1%), this compact representation, combined with our strong geometric priors, effectively prevents overfitting and enables rapid convergence. When supervision increases to 10%, the additional data provides sufficient gradient signals for heavier models to leverage the higher capacity of their dense token spaces, marginally closing the performance gap. Nevertheless, SLiM still achieves strictly comparable or superior results while requiring a drastically reduced computational footprint.

Action retrieval. To further evaluate the discriminative capability of the learned representations, we conduct action retrieval experiments on the NTU-60 dataset using a k -Nearest Neighbor (k -NN) classifier ($k = 1$). Table 4 shows the performance comparison for skeleton-based action retrieval against various state-of-the-art methods. Unlike the linear evaluation protocol, this task assesses the features without any additional supervised training, thereby serving as a direct measure of the inherent semantic quality and generalization of the frozen backbone. As summarized in Table 4, our SLiM framework consistently outperforms all state-of-the-art competitors by a clear margin. These results confirm that our framework learns more semantically robust and well-clustered representations, making them highly suitable for retrieval tasks even in a non-parametric setting.

4.4 Ablation Studies

We conduct extensive ablation studies on the NTU-60. For computational efficiency, all ablation models are pre-trained for 100 epochs, whereas our final full model is trained for 150 epochs. In the following analyses, the term “*Limited*” refers to the conventional masking and augmentations illustrated in Fig. 3-(a-d).

Impact of the unified framework. Table 5 evaluates the synergy between \mathcal{L}_{MFM} and $\mathcal{L}_{\text{GLCL}}$. First, relying exclusively on \mathcal{L}_{MFM} lacks the instance-level

Table 7: Ablation studies for the SAA on NTU-60. We evaluate the contribution of each component: skeleton-aware rotation, skeleton-aware mirroring, and bone-aware scaling. Limited: previous augmentation methods as depicted in Fig. 3.

Rotation	Mirroring	Scaling	X-Sub	X-View
\times	\checkmark	\checkmark	81.6	86.9
\checkmark (Limited)	\checkmark	\checkmark	84.8	89.9
\checkmark	\times	\checkmark	85.3	90.6
\checkmark	\checkmark (Limited)	\checkmark	85.9	91.0
\checkmark	\checkmark	\times	84.4	90.0
\checkmark	\checkmark	\checkmark (Limited)	86.4	91.7
\checkmark	\checkmark	\checkmark	87.7	92.7

discriminative capability required for distinct action boundaries, saturating at 85.3% on X-Sub. To address this, augmenting the model with a standard contrastive approach (\mathcal{L}_{CL})—which generates the same number of views but strictly bounds them to 16-frame clips—yields a suboptimal 86.2% on X-Sub. This limitation occurs because robust action understanding necessitates learning from multiple temporal scales, rather than being confined to a single, rigid clip length. Our \mathcal{L}_{GLCL} resolves this via hierarchical temporal sampling, ensuring semantic alignment across diverse temporal granularities. Ultimately, integrating \mathcal{L}_{MFM} and \mathcal{L}_{GLCL} within a single decoder-free framework guides the shared encoder to simultaneously master fine-grained feature modeling and scale-invariant discrimination, thereby achieving peak performance (87.7% on X-Sub) and validating their complementary nature.

Efficacy of dual-role STM. Table 6 demonstrates the impact of our masking strategies. When applying the independent joint masking common in prior works [1, 22, 32], the model easily cheats the pretext task via spatial interpolation from adjacent coordinates. Consequently, utilizing this limited strategy yields suboptimal performance: 84.2% on X-Sub for the global view (\mathcal{L}_{MFM} target) and 85.7% for the local view (\mathcal{L}_{GLCL} perturbation). In contrast, our STM prevents such naive shortcut learning by masking entire anatomical parts across the temporal axis. STM serves a dual role: providing robust targets for \mathcal{L}_{MFM} and acting as a strong structural perturbation for \mathcal{L}_{GLCL} . By driving the encoder to deeply understand motion dynamics, integrating STM across both objectives achieves a peak performance of 87.7%, demonstrating substantial improvements (+3.5%-point and +2.0%-point, respectively) over conventional masking.

Impact of SAA. Table 7 isolates the contributions of geometric augmentations. By substituting standard augmentations from prior works [11, 17] with our SAA—encompassing skeleton-aware rotation, mirroring, and bone-aware scaling—we strictly preserve the 3D geometric validity of contrastive pairs. This anatomical consistency directly translates to enhanced downstream accuracy. Consequently, compared to their conventional counterparts, our rotation, mirroring, and scaling yield substantial improvements of +2.9%-point, +1.8%-point, and +1.3%-point on X-Sub, respectively.

5 Conclusion

In this work, we present **SLiM**, a unified framework that harmonizes masked modeling with contrastive learning to overcome the granularity-efficiency trade-off in prior work. By adopting a decoder-free student-teacher architecture, SLiM eliminates computational redundancy while capturing discriminative features via *Semantic Tube Masking* and *Skeletal-Aware Augmentations*. Extensive experiments demonstrate that SLiM consistently achieves state-of-the-art performance across all downstream tasks using only joint modality. Notably, our method delivers this superior accuracy with exceptional efficiency, reducing inference complexity by $7.89\times$. SLiM establishes a scalable paradigm for real-world action recognition, proving that robust representation can indeed be achieved with significantly less computational cost.

Acknowledgements

This work was supported by IITP grant funded by the Korea government (MSIT) (No.RS2022-00144444, Deep Learning Based Visual Representational Learning and Rendering of Static and Dynamic Scenes).

Appendix Overview

Section	Descriptions for Analysis and Discussion
Sec. A	Implementation Details: Architecture, loss functions, and hyper-parameters
Sec. B	Hierarchical Temporal Sampling: Global/local view generation
Sec. C	Semantic Tube Masking (STM) (Algorithm 1)
Sec. D	Skeleton-Aware Augmentations (SAA): Rotation (Algorithm 2), mirroring (Algorithm 3), and scaling (Algorithm 4)
Sec. E	Additional Results and Discussion: Transfer learning evaluation on PKU-MMD II [18] (Table 8)

This *Appendix* provides comprehensive technical and algorithmic details for the SLiM framework. We begin in Sec. A by elaborating on the implementation details, including the specific network architecture, loss function formulations, and hyper-parameter configurations used throughout our experiments. In Sec. B, we describe the hierarchical temporal sampling strategy, which explains the generation of global and local views to maintain semantic consistency. The formal algorithmic procedures for our core modules are then detailed: Sec. C presents the Semantic Tube Masking (STM), while Sec. D provides the suite of Skeleton-Aware Augmentations (SAA), specifically covering rotation, mirroring, and scaling algorithms. Finally, Sec. E concludes with additional results and discussions, including transfer learning evaluations.

A Implementation Details

Detailed architecture. Our encoder g follows a ViT [8] variant optimized for skeleton data, consisting of 8 Transformer layers with a hidden dimension of $D = 256$ and 8 attention heads. To enhance the stability of attention maps and prevent feature collapse, we introduce 4 register tokens ($N_{\text{reg}} = 4$) [5], which allows the model to isolate outlier features. Both student network f_{θ} and teacher network f_{ϕ} utilize identical 3-layer MLP projection heads (h_{CL} and h_{MAE}) with a hidden dimension of 2,048 and a bottleneck dimension of 256. These heads project features onto a high-dimensional prototype space of $K = 65,536$ dimensions to facilitate fine-grained feature discrimination. Consequently, the probability distributions \mathbf{p} in Eq. 4 and Eq. 6 are defined over this K -dimensional categorical space, forcing the model to distinguish between tens of thousands of refined motion patterns.

Loss functions. The total loss is optimized by balancing the masked feature modeling loss \mathcal{L}_{MFM} and the global-local contrastive loss $\mathcal{L}_{\text{GLCL}}$ with an equal weight of 1:1, setting the hyperparameter $\lambda = 1$ in Eq. 7. Additionally, we incorporate the KoLeo loss [24] with a weight of 0.1 to encourage the local features to be spread uniformly across the unit sphere, further enhancing the

discriminative power of the learned representations. For prototype centering, we adopt the Sinkhorn-Knopp algorithm [24, 42] to ensure a uniform distribution of assignments across the prototype space.

B Hierarchical Temporal Sampling

To learn robust representations that are invariant to temporal scale variations, SLiM employs a hierarchical temporal sampling strategy. This approach ensures that all generated views maintain semantic consistency by anchoring short-term local clips within the temporal boundaries of long-term global segments. Specifically, *for all views, we first define the target temporal interval and then perform uniform sampling within that segment* to extract the required constituent frames. Crucially, if the sampled physical duration is shorter than the target number of frames, we apply linear temporal interpolation to resize the clip to its designated resolution (64, 32, 16, or 8 frames). This two-step process—segment definition followed by uniform sampling—ensures a balanced representation of action dynamics across varying temporal scales.

Global view sampling. We first generate two global views, \mathbf{X}_{G1} and \mathbf{X}_{G2} , by randomly selecting temporal intervals from the raw skeleton sequence, which are then uniformly sampled to $T = 64$ frames. The duration of these global intervals is uniformly random sampled to cover between 50% and 100% of the total sequence length T_{input} (i.e., $0.5 < (t_{\text{end}} - t_{\text{start}})/T_{\text{input}} < 1.0$). This ensures that the global views capture the primary action context while providing sufficient variety for instance-level discrimination.

Local view sampling. As illustrated in Fig. 2, local views ($\mathbf{X}_{L1}, \mathbf{X}_{L2}, \mathbf{X}_{L3}$) are re-sampled from the specific temporal interval $[t_{\text{start}}^1, t_{\text{end}}^1]$ assigned to the primary global anchor \mathbf{X}_{G1} . This constraint is vital to prevent semantic misalignment, where distant clips from the same sequence might depict unrelated motion states. For each resolution, we extract two independent crops, with the relative interval ratio p (proportion of the global interval) defined as follows:

- 32-frame views (\mathbf{X}_{L1}): We sample two crops where each clip’s duration is 35% to 70% of the global anchor interval (i.e., $p \in [0.35, 0.7]$).
- 16-frame views (\mathbf{X}_{L2}): We sample two crops where each clip’s duration is 15% to 40% of the global anchor interval (i.e., $p \in [0.15, 0.4]$).
- 8-frame views (\mathbf{X}_{L3}): We sample two crops where each clip’s duration is 5% to 20% of the global anchor interval (i.e., $p \in [0.05, 0.2]$).

C Semantic Tube Masking (STM)

Concept and motivation. As shown in Fig. 3, independent joint masking [1, 22, 32, 38] often permits the model to bypass robust representation learning by simply interpolating missing coordinates from immediate spatial neighbors. To prevent this trivial shortcut reconstruction, Semantic Tube Masking (STM) explicitly masks integral anatomical groups (e.g., arms, legs, or torso) continuously

Algorithm 1 Semantic Tube Masking (STM)

Input: Target total number of masked elements N_{mask} , temporal length T , number of joints J , set of semantic joint groups $\mathcal{G} = \{G_1, G_2, \dots, G_K\}$, minimum and maximum mask area per step $A_{\text{min}}, A_{\text{max}}$.

Initialization:

- 1: Initialize boolean mask $\mathcal{M} \in \{0, 1\}^{T \times J}$ with zeros.
- 2: Initialize current masked element count $C = 0$.

Semantic Tube Mask Generation:

- 3: **while** $C < N_{\text{mask}}$ **do** \triangleright Iteratively generate mask tubes until target is met
- 4: Calculate max allowed patches for current step: $P_{\text{max}} = \min(N_{\text{mask}} - C, A_{\text{max}})$.

Step 1. Skeletal Selection (Joints):

- 5: Randomly select a semantic joint group $G \in \mathcal{G}$.
- 6: Randomly select a *contiguous* subset of joints $S \subseteq G$. Let width $w = |S|$.

Step 2. Temporal Selection (Frames):

- 7: Sample target mask area $A \sim \mathcal{U}(A_{\text{min}}, P_{\text{max}})$.
- 8: Calculate temporal duration $h = \min(\max(\text{round}(A/w), 1), T)$.
- 9: Randomly sample starting temporal index $t \sim \mathcal{U}(0, T - h)$.

Step 3. Apply Mask:

- 10: Apply mask: $\mathcal{M}[t : t + h, S] \leftarrow 1$.
- 11: Update the total mask count: $C \leftarrow \sum_{t,j} \mathcal{M}[t, j]$.
- 12: **end while**

Output: Semantic Tube Mask \mathcal{M}

across the temporal dimension, thereby forming continuous skeletal-temporal tubes.

Anatomical joint grouping. To implement this on standard 25-joint skeleton sequences (e.g., the Kinect v2 topology utilized in the NTU-60 [26], NTU-120 [19], and PKU-MMD II [18] datasets), we define the set of semantic joint groups \mathcal{G} by dividing the human body into five distinct anatomical regions: Torso $G_1 = \{0, 1, 20, 2, 3\}$, Left Arm $G_2 = \{4, 5, 6, 7, 21, 22\}$, Right Arm $G_3 = \{8, 9, 10, 11, 23, 24\}$, Left Leg $G_4 = \{12, 13, 14, 15\}$, and Right Leg $G_5 = \{16, 17, 18, 19\}$. To ensure that masking does not degrade into independent joint occlusion within these regions, we randomly select a *anatomically contiguous* (i.e., skeletally connected) subset of joints $S \subseteq G$ to form the spatial mask. For example, rather than dropping disconnected joints from the Left Arm G_2 , we select a contiguous sequence (e.g., the elbow, wrist, and hand joints $\{5, 6, 7\}$), guaranteeing that a connected spatial block is occluded and preventing trivial interpolation.

Constant tube volume strategy. Algorithm 1 details the procedure for our constant tube volume strategy, which is designed to balance the masking dif-

ficuity across different body parts. Specifically, the temporal duration h of the applied mask is calculated inversely proportional to the spatial width w of the selected joint group $S \subseteq G$. Consequently, smaller anatomical groups are occluded over longer temporal spans, whereas larger groups are masked for shorter intervals.

Mask generation parameters. During the iterative mask generation process, the bounding parameters for the mask area per step are controlled. We set the minimum mask area per step to $A_{\min} = 8$ and restrict the maximum area per step to half of the sequence, $A_{\max} = 0.5N$, where $N = (T/P_T) \times (J/P_J)$ denotes the total number of skeletal-temporal tokens. For every generated mask \mathcal{M} , the total target masking ratio is uniformly sampled such that the final number of masked elements N_{mask} consistently ranges between 50% and 90% of the total tokens (i.e., $N_{\text{mask}} \in [0.5N, 0.9N]$).

Dual-role application. \mathcal{M} serves a dual purpose in our framework, applied with varying probabilities depending on the view being processed. For the primary global view, the mask is always applied (probability of $p = 1.0$) because it directly constructs the corrupted input required for the Masked Feature Modeling (MFM) objective. Conversely, for the local views leveraged in the Global-Local Contrastive Learning (GLCL) branch, STM is applied stochastically with a probability of $p = 0.5$, functioning as a hard structural perturbation to further enhance representation robustness.

D Skeleton-Aware Augmentations (SAA)

As illustrated in Fig. 3, standard geometric transformations [11, 17, 45] frequently overlook the physical constraints of articulated human bodies, resulting in distorted limb proportions or physically implausible postures. Our SAA framework addresses this limitation by constructing diverse yet structurally valid contrastive pairs. To ensure sufficient view diversity while maintaining anatomical integrity, each augmentation within the SAA suite is applied independently with a probability of $p = 0.5$.

D.1 Skeleton-Aware Rotation (Algorithm 2)

Traditional uniform rotation strategies [4, 11, 17] are typically restricted to narrow angle ranges to avoid unrealistic poses. Our approach explicitly decouples the rotation logic. Specifically, we sample the vertical rotation angle β from a uniform distribution $\mathcal{U}(-\theta_{\text{vert}}, \theta_{\text{vert}})$ with $\theta_{\text{vert}} = 180^\circ$, effectively applying a full 360° random rotation exclusively around the vertical Y -axis to preserve a realistic upright posture. Conversely, the tilt angles α and γ along the non-gravity axes (X and Z , respectively) are sampled from $\mathcal{U}(-\theta_{\text{tilt}}, \theta_{\text{tilt}})$. We bound these perturbations to small angles by setting $\theta_{\text{tilt}} = 30^\circ$ to prevent physically impossible tilting.

Algorithm 2 Skeleton-Aware Rotation

Input: Skeleton sequence $\mathbf{X} \in \mathbb{R}^{C \times T \times J}$, tilt angle limit θ_{tilt} , vertical rotation limit θ_{vert} .

Step 1. Sample Rotation Angles:

- 1: Sample X-axis tilt angle $\alpha \sim \mathcal{U}(-\theta_{\text{tilt}}, \theta_{\text{tilt}})$.
- 2: Sample Y-axis vertical angle $\beta \sim \mathcal{U}(-\theta_{\text{vert}}, \theta_{\text{vert}})$. ▷ Typically large, e.g., 180°
- 3: Sample Z-axis tilt angle $\gamma \sim \mathcal{U}(-\theta_{\text{tilt}}, \theta_{\text{tilt}})$.

Step 2. Construct Rotation Matrix:

- 4: Compute 3D rotation matrices $\mathbf{R}_x(\alpha)$, $\mathbf{R}_y(\beta)$, and $\mathbf{R}_z(\gamma)$.
- 5: Combine into a single rotation matrix: $\mathbf{R} = \mathbf{R}_z \mathbf{R}_y \mathbf{R}_x \in \mathbb{R}^{3 \times 3}$.

Step 3. Apply Rotation:

- 6: Transform the coordinates for all joints:
 $\mathbf{X}_{\text{rot}}[:, t, j] = \mathbf{R}\mathbf{X}[:, t, j]$ for all $t \in \{0, \dots, T-1\}$ and $j \in \{0, \dots, J-1\}$.

Output: Rotated sequence \mathbf{X}_{rot}

D.2 Skeleton-Aware Mirroring (Algorithm 3)

Conventional index swapping [6, 11, 17] fails to execute a mathematically rigorous reflection, leading to unnatural motion artifacts. Our geometric mirroring strategy simultaneously negates the spatial coordinate values along the lateral X-axis and reassigns the corresponding left-right joint indices via a predefined bilateral mapping $\mathcal{I}_{\text{swap}}$. Specifically, for the standard 25-joint Kinect v2 topology utilized in the NTU-60 [26], NTU-120 [19], and PKU-MMD II [18] datasets, $\mathcal{I}_{\text{swap}}$ explicitly swaps the symmetric anatomical pairs across the body’s vertical midline: the arms $\{(5, 9), (6, 10), (7, 11), (8, 12)\}$, the legs $\{(13, 17), (14, 18), (15, 19), (16, 20)\}$, and the hands $\{(22, 24), (23, 25)\}$, while central spine and head joints remain at their original indices. This dual operation—spatial negation coupled with rigorous index swapping—guarantees that the left-right semantics and the correct “Front” orientation are anatomically preserved.

D.3 Bone-Aware Scaling (Algorithm 4)

Naive scaling of raw joint coordinates can severely disrupt the structural integrity of the skeletal topology. To simulate actions performed by subjects of varying body sizes without inducing semantic distortion, we apply scaling operations directly in the bone vector space. We first decompose the skeleton into independent bone vectors and sample random scaling factors s_G uniformly from the range $[0.85, 1.15]$ ($s_{\text{min}} = 0.85$ and $s_{\text{max}} = 1.15$). These factors are then applied to the bone lengths, ensuring their directional unit vectors \hat{v} are fully preserved. The final joint coordinates are then iteratively reconstructed in topological order starting from the root joint trajectory.

Algorithm 3 Skeleton-Aware Mirroring

Input: Skeleton sequence $\mathbf{X} \in \mathbb{R}^{C \times T \times J}$, predefined left-right joint swapping mapping $\mathcal{I}_{\text{swap}}$.

Step 1. Joint Index Swapping:

- 1: Swap the left and right anatomical joints based on the mapping:
 $\mathbf{X}_{\text{swap}}[:, :, j] = \mathbf{X}[:, :, \mathcal{I}_{\text{swap}}(j)]$ for all $j \in \{0, \dots, J - 1\}$.

Step 2. Spatial Reflection:

- 2: Invert the coordinates along the X -axis (Horizontal mirroring):
 $\mathbf{X}_{\text{mirror}}[0, :, :] = -\mathbf{X}_{\text{swap}}[0, :, :]$. \triangleright Assuming channel 0 corresponds to the X -axis

Output: Mirrored sequence $\mathbf{X}_{\text{mirror}}$

E Additional Results and Discussion

E.1 Transfer Learning Evaluation

To assess the generalizability of the learned action representations, we conduct a transfer learning evaluation following the established protocol in recent literature. In this scenario, the SLiM encoder g is first pre-trained on a large-scale source dataset using our self-supervised framework. The frozen encoder is then evaluated on a different target dataset using the linear evaluation mechanism where only a single linear classifier is trained on top of the fixed representations without additional fine-tuning. This process verifies whether the model has captured universal motion semantics that are robust to domain shifts and varying skeleton topologies. Table 8 shows the transfer learning performance on PKU-MMD II [18] dataset. As shown, SLiM demonstrates superior transferability across all tested scenarios compared to previous state-of-the-art methods. Specifically, when pre-trained on the NTU-120 [19] X-Sub split, SLiM achieves a peak accuracy of 75.3%, outperforming S-JEPA [1] by 1.1%-point. These results highlight that the representations learned via our Semantic Tube Masking (STM) and Global-Local Contrastive Learning (GLCL) objectives are more context-rich and transferable than those focusing on low-level coordinate reconstruction. By effectively predicting high-dimensional latent features, SLiM establishes a more robust anatomical understanding, ensuring that the captured motion patterns generalize effectively across different datasets and subject distributions.

Algorithm 4 Bone-Aware Scaling

Input: Skeleton sequence $\mathbf{X} \in \mathbb{R}^{C \times T \times J}$, parent joint mapping \mathcal{P} , semantic joint groups \mathcal{G} , scale range $[s_{\min}, s_{\max}]$.

Step 1. Joint to Bone Conversion:

- 1: The root bone is initialized to zero: $\mathbf{B}[:, :, 0] = \mathbf{0}$.
- 2: Extract bone vectors \mathbf{B} from joints \mathbf{X} . For each joint $j \in \{1, \dots, J-1\}$:
 $\mathbf{B}[:, :, j] = \mathbf{X}[:, :, j] - \mathbf{X}[:, :, \mathcal{P}(j)]$.

Step 2. Generate Independent Scale Factors:

- 3: Initialize scale factor matrix $\mathbf{S} \in \mathbb{R}^J$.
- 4: **for** each group $G \in \mathcal{G}$ **do**
- 5: Sample a scale factor $s_G \sim \mathcal{U}(s_{\min}, s_{\max})$.
- 6: Assign s_G to all joints in group G : $\mathbf{S}[j] = s_G$ for $j \in G$.
- 7: **end for**

Step 3. Apply Bone Scaling:

- 8: Scale the bone vectors for :
 $\mathbf{B}_{\text{scale}}[:, :, j] = \mathbf{B}[:, :, j] \odot \mathbf{S}[j]$. $\triangleright \odot$ denotes element-wise multiplication

Step 4. Reconstruct Joints:

- 9: Initialize $\mathbf{X}_{\text{scale}}$ and preserve the original root joint trajectory:
 $\mathbf{X}_{\text{scale}}[:, :, 0] = \mathbf{X}[:, :, 0]$.
- 10: **for** each joint $j \in \{1, \dots, J-1\}$ in topological order **do**
- 11: Recover joint positions:
 $\mathbf{X}_{\text{scale}}[:, :, j] = \mathbf{X}_{\text{scale}}[:, :, \mathcal{P}(j)] + \mathbf{B}_{\text{scale}}[:, :, j]$
- 12: **end for**

Output: Scaled sequence $\mathbf{X}_{\text{scale}}$

Table 8: *Transfer learning* performance on PKU-MMD II. We evaluate cross-dataset generalization by pre-training on the *Cross-Subject (X-Sub)* splits of NTU-60 and NTU-120, and testing on the PKU-MMD II X-Sub dataset. **Bold** and underline indicate the best and second-best results, respectively.

Method	To PKU-II	
	NTU-60	NTU-120
LongT-GAN [41]	44.8	–
ISC [29]	51.1	52.3
CMD [23]	56.0	57.0
MacDiff [37]	<u>72.2</u>	73.4
IGM [16]	59.8	–
SkeletonMAE [38]	58.4	61.0
MAMP [22]	70.6	73.2
S-JEPA [1]	71.4	<u>74.2</u>
SLiM (Ours)	72.7	75.3

References

1. Abdelfattah, M., Alahi, A.: S-jepa: A joint embedding predictive architecture for skeletal action recognition. In: European Conference on Computer Vision. pp. 367–384. Springer (2024)
2. Caron, M., Touvron, H., Misra, I., Jégou, H., Mairal, J., Bojanowski, P., Joulin, A.: Emerging properties in self-supervised vision transformers. In: Proceedings of the IEEE/CVF international conference on computer vision. pp. 9650–9660 (2021)
3. Chen, T., Kornblith, S., Norouzi, M., Hinton, G.: A simple framework for contrastive learning of visual representations. In: International conference on machine learning. pp. 1597–1607. PmLR (2020)
4. Chen, Y., Zhang, Z., Yuan, C., Li, B., Deng, Y., Hu, W.: Channel-wise topology refinement graph convolution for skeleton-based action recognition. In: Proceedings of the IEEE/CVF international conference on computer vision. pp. 13359–13368 (2021)
5. Darcet, T., Oquab, M., Mairal, J., Bojanowski, P.: Vision transformers need registers. arXiv preprint arXiv:2309.16588 (2023)
6. Do, J., Kim, M.: Skateformer: skeletal-temporal transformer for human action recognition. In: European Conference on Computer Vision. pp. 401–420. Springer (2024)
7. Dong, J., Sun, S., Liu, Z., Chen, S., Liu, B., Wang, X.: Hierarchical contrast for unsupervised skeleton-based action representation learning. In: Proceedings of the AAAI Conference on Artificial Intelligence. vol. 37, pp. 525–533 (2023)
8. Dosovitskiy, A., Beyer, L., Kolesnikov, A., Weissenborn, D., Zhai, X., Unterthiner, T., Dehghani, M., Minderer, M., Heigold, G., Gelly, S., et al.: An image is worth 16x16 words: Transformers for image recognition at scale. arXiv preprint arXiv:2010.11929 (2020)
9. Duan, H., Zhao, Y., Chen, K., Lin, D., Dai, B.: Revisiting skeleton-based action recognition. In: Proceedings of the IEEE/CVF conference on computer vision and pattern recognition. pp. 2969–2978 (2022)
10. Franco, L., Mandica, P., Munjal, B., Galasso, F.: Hyperbolic self-paced learning for self-supervised skeleton-based action representations. arXiv preprint arXiv:2303.06242 (2023)
11. Guo, T., Liu, H., Chen, Z., Liu, M., Wang, T., Ding, R.: Contrastive learning from extremely augmented skeleton sequences for self-supervised action recognition. In: Proceedings of the AAAI Conference on Artificial Intelligence. vol. 36, pp. 762–770 (2022)
12. He, K., Chen, X., Xie, S., Li, Y., Dollár, P., Girshick, R.: Masked autoencoders are scalable vision learners. In: Proceedings of the IEEE/CVF conference on computer vision and pattern recognition. pp. 16000–16009 (2022)
13. Hua, Y., Wu, W., Zheng, C., Lu, A., Liu, M., Chen, C., Wu, S.: Part aware contrastive learning for self-supervised action recognition. arXiv preprint arXiv:2305.00666 (2023)
14. Kim, B., Chang, H.J., Kim, J., Choi, J.Y.: Global-local motion transformer for unsupervised skeleton-based action learning. In: European conference on computer vision. pp. 209–225. Springer (2022)
15. Kong, Y., Fu, Y.: Human action recognition and prediction: A survey. International Journal of Computer Vision **130**(5), 1366–1401 (2022)
16. Lin, L., Wu, L., Zhang, J., Liu, J.: Idempotent unsupervised representation learning for skeleton-based action recognition. In: European Conference on Computer Vision. pp. 75–92. Springer (2024)

17. Lin, L., Zhang, J., Liu, J.: Actionlet-dependent contrastive learning for unsupervised skeleton-based action recognition. In: Proceedings of the IEEE/CVF Conference on Computer Vision and Pattern Recognition. pp. 2363–2372 (2023)
18. Liu, C., Hu, Y., Li, Y., Song, S., Liu, J.: Pku-mmd: A large scale benchmark for continuous multi-modal human action understanding. arXiv preprint arXiv:1703.07475 (2017)
19. Liu, J., Shahroudy, A., Perez, M., Wang, G., Duan, L.Y., Kot, A.C.: Ntu rgb+ d 120: A large-scale benchmark for 3d human activity understanding. *IEEE transactions on pattern analysis and machine intelligence* **42**(10), 2684–2701 (2019)
20. Loshchilov, I., Hutter, F.: Sgdr: Stochastic gradient descent with warm restarts. arXiv preprint arXiv:1608.03983 (2016)
21. Loshchilov, I., Hutter, F.: Decoupled weight decay regularization. arXiv preprint arXiv:1711.05101 (2017)
22. Mao, Y., Deng, J., Zhou, W., Fang, Y., Ouyang, W., Li, H.: Masked motion predictors are strong 3d action representation learners. In: Proceedings of the IEEE/CVF International Conference on Computer Vision. pp. 10181–10191 (2023)
23. Mao, Y., Zhou, W., Lu, Z., Deng, J., Li, H.: Cmd: Self-supervised 3d action representation learning with cross-modal mutual distillation. In: European Conference on Computer Vision. pp. 734–752. Springer (2022)
24. Oquab, M., Darcet, T., Moutakanni, T., Vo, H., Szafraniec, M., Khalidov, V., Fernandez, P., Haziza, D., Massa, F., El-Nouby, A., et al.: Dinov2: Learning robust visual features without supervision. arXiv preprint arXiv:2304.07193 (2023)
25. Shah, A., Roy, A., Shah, K., Mishra, S., Jacobs, D., Cherian, A., Chellappa, R.: Halp: Hallucinating latent positives for skeleton-based self-supervised learning of actions. In: Proceedings of the IEEE/CVF Conference on Computer Vision and Pattern Recognition. pp. 18846–18856 (2023)
26. Shahroudy, A., Liu, J., Ng, T.T., Wang, G.: Ntu rgb+ d: A large scale dataset for 3d human activity analysis. In: Proceedings of the IEEE conference on computer vision and pattern recognition. pp. 1010–1019 (2016)
27. Su, J., Ahmed, M., Lu, Y., Pan, S., Bo, W., Liu, Y.: Roformer: Enhanced transformer with rotary position embedding. *Neurocomputing* **568**, 127063 (2024)
28. Su, K., Liu, X., Shlizerman, E.: Predict & cluster: Unsupervised skeleton based action recognition. In: Proceedings of the IEEE/CVF conference on computer vision and pattern recognition. pp. 9631–9640 (2020)
29. Su, K., Liu, X., Shlizerman, E.: Predict & cluster: Unsupervised skeleton based action recognition. In: Proceedings of the IEEE/CVF conference on computer vision and pattern recognition. pp. 9631–9640 (2020)
30. Sun, K., Xiao, B., Liu, D., Wang, J.: Deep high-resolution representation learning for human pose estimation. In: Proceedings of the IEEE/CVF conference on computer vision and pattern recognition. pp. 5693–5703 (2019)
31. Sun, S., Liu, D., Dong, J., Qu, X., Gao, J., Yang, X., Wang, X., Wang, M.: Unified multi-modal unsupervised representation learning for skeleton-based action understanding. In: Proceedings of the 31st ACM International Conference on Multimedia. pp. 2973–2984 (2023)
32. Sun, S., Zhang, Z., Dong, J., Cheng, Z., Chang, X., Wang, M.: Towards efficient general feature prediction in masked skeleton modeling. In: Proceedings of the IEEE/CVF International Conference on Computer Vision. pp. 12212–12221 (2025)
33. Sun, Z., Ke, Q., Rahmani, H., Bennamoun, M., Wang, G., Liu, J.: Human action recognition from various data modalities: A review. *IEEE transactions on pattern analysis and machine intelligence* **45**(3), 3200–3225 (2022)

34. Tarvainen, A., Valpola, H.: Mean teachers are better role models: Weight-averaged consistency targets improve semi-supervised deep learning results. *Advances in neural information processing systems* **30** (2017)
35. Wang, H., Ma, X., Kuang, J., Gui, J.: Heterogeneous skeleton-based action representation learning. In: *Proceedings of the Computer Vision and Pattern Recognition Conference*. pp. 19154–19164 (2025)
36. Weng, W., Wang, H., Wang, J., He, L., Xie, G.S.: Usdrl: Unified skeleton-based dense representation learning with multi-grained feature decorrelation. In: *Proceedings of the AAAI Conference on Artificial Intelligence*. vol. 39, pp. 8332–8340 (2025)
37. Wu, L., Lin, L., Zhang, J., Ma, Y., Liu, J.: Macdiff: Unified skeleton modeling with masked conditional diffusion. In: *European Conference on Computer Vision*. pp. 110–128. Springer (2024)
38. Wu, W., Hua, Y., Zheng, C., Wu, S., Chen, C., Lu, A.: Skeletonmae: Spatial-temporal masked autoencoders for self-supervised skeleton action recognition. In: *2023 IEEE international conference on multimedia and expo workshops (ICMEW)*. pp. 224–229. IEEE (2023)
39. Zhang, H., Hou, Y., Zhang, W., Li, W.: Contrastive positive mining for unsupervised 3d action representation learning. In: *European Conference on Computer Vision*. pp. 36–51. Springer (2022)
40. Zhang, J., Lin, L., Yang, S., Liu, J.: Self-supervised skeleton-based action representation learning: A benchmark and beyond: J. zhang et al. *International Journal of Computer Vision* **134**(1), 38 (2026)
41. Zheng, N., Wen, J., Liu, R., Long, L., Dai, J., Gong, Z.: Unsupervised representation learning with long-term dynamics for skeleton based action recognition. In: *Proceedings of the AAAI conference on artificial intelligence*. vol. 32 (2018)
42. Zhou, J., Wei, C., Wang, H., Shen, W., Xie, C., Yuille, A., Kong, T.: ibot: Image bert pre-training with online tokenizer. *arXiv preprint arXiv:2111.07832* (2021)
43. Zhou, Y., Duan, H., Rao, A., Su, B., Wang, J.: Self-supervised action representation learning from partial spatio-temporal skeleton sequences. In: *Proceedings of the AAAI conference on artificial intelligence*. vol. 37, pp. 3825–3833 (2023)
44. Zhu, Y., Han, H., Yu, Z., Liu, G.: Modeling the relative visual tempo for self-supervised skeleton-based action recognition. In: *Proceedings of the IEEE/CVF International Conference on Computer Vision*. pp. 13913–13922 (2023)
45. Zolfaghari, M., Zhu, Y., Gehler, P., Brox, T.: Crossclr: Cross-modal contrastive learning for multi-modal video representations. In: *Proceedings of the IEEE/CVF international conference on computer vision*. pp. 1450–1459 (2021)